Research Article | Vol. 7, No. 11 | 1 Nov 2016 | BIOMEDICAL OPTICS EXPRESS 4639

Biomedical Optics EXPRESS

Kagome fiber based ultrafast laser microsurgery probe delivering micro-Joule pulse energies

KAUSHIK SUBRAMANIAN,[1,4] ILAN GABAY,[1,4] ONUR FERHANOĞLU,[1] ADAM SHADFAN,[2] MICHAL PAWLOWSKI,[2] YE WANG,[2] TOMASZ TKACZYK,[2] AND ADELA BEN-YAKAR[1,3,*]

[1]*Department of Mechanical Engineering, The University of Texas at Austin, Texas 78712, USA*
[2]*Department of Bioengineering, Rice University, Houston 77005, USA*
[3]*Department of Biomedical Engineering, The University of Texas at Austin, Texas 78712, USA*
[4]*These authors contributed equally to this work*
[*]*ben-yakar@mail.utexas.edu*

Abstract: We present the development of a 5 mm, piezo-actuated, ultrafast laser scalpel for fast tissue microsurgery. Delivery of micro-Joules level energies to the tissue was made possible by a large, 31 μm, air-cored inhibited-coupling Kagome fiber. We overcome the fiber's low NA by using lenses made of high refractive index ZnS, which produced an optimal focusing condition with 0.23 NA objective. The optical design achieved a focused laser spot size of 4.5 μm diameter covering a 75 × 75 μm^2 scan area in a miniaturized setting. The probe could deliver the maximum available laser power, achieving an average fluence of 7.8 J/cm^2 on the tissue surface at 62% transmission efficiency. Such fluences could produce uninterrupted, 40 μm deep cuts at translational speeds of up to 5 mm/s along the tissue. We predicted that the best combination of speed and coverage exists at 8 mm/s for our conditions. The onset of nonlinear absorption in ZnS, however, limited the probe's energy delivery capabilities to 1.4 μJ for linear operation at 1.5 picosecond pulse-widths of our fiber laser. Alternatives like broadband CaF_2 crystals should mitigate such nonlinear limiting behavior. Improved opto-mechanical design and appropriate material selection should allow substantially higher fluence delivery and propel such Kagome fiber-based scalpels towards clinical translation.

OCIS codes: (170.1020) Ablation of tissue; (140.7090) Ultrafast lasers; (190.4400) Nonlinear optics, materials; (170.3890) Medical optics instrumentation; (190.4370) Nonlinear optics, fibers.

References and links

1. A. Vogel and V. Venugopalan, "Mechanisms of pulsed laser ablation of biological tissues," Chem. Rev. **103**(2), 577–644 (2003).
2. G. Chen, *Nanoscale Energy Transport and Conversion* (Oxford University Press, 2005).
3. I. Ratkay-Traub, I. E. Ferincz, T. Juhasz, R. M. Kurtz, and R. R. Krueger, "First clinical results with the femtosecond neodynium-glass laser in refractive surgery," J. Refract. Surg. **19**(2), 94–103 (2003).
4. T. Juhasz, F. H. Loesel, R. M. Kurtz, C. Horvath, J. F. Bille, and G. Mourou, "Corneal refractive surgery with femtosecond lasers," IEEE J. Sel. Top. Quantum Electron. **5**(4), 902–910 (1999).
5. J. Wang, G. Schuele, and D. Palanker, "Finesse of transparent tissue cutting by ultrafast lasers at various wavelengths," J. Biomed. Opt. **20**(12), 125004 (2015).
6. N. Nishimura, C. B. Schaffer, B. Friedman, P. S. Tsai, P. D. Lyden, and D. Kleinfeld, "Targeted insult to subsurface cortical blood vessels using ultrashort laser pulses: three models of stroke," Nature Methods **3**, 5–7 (2006).
7. K. S. Frederickson, W. E. White, R. G. Wheeland, and D. R. Slaughter, "Precise ablation of skin with reduced collateral damage using the femtosecond-pulsed, terawatt titanium-sapphire laser," Arch. Dermatol. **129**(8), 989–993 (1993).
8. J. Neev, J. S. Nelson, M. Critelli, J. L. McCullough, E. Cheung, W. A. Carrasco, A. M. Rubenchik, L. B. Da Silva, M. D. Perry, and B. C. Stuart, "Ablation of human nail by pulsed lasers," Lasers Surg. Med. **21**(2), 186–192 (1997).
9. J. Neev, L. H. Liaw, D. V. Raney, J. T. Fujishige, P. D. Ho, and M. W. Berns, "Selectivity, efficiency, and

#275155 http://dx.doi.org/10.1364/BOE.7.004639
Journal © 2016 Received 2 Sep 2016; revised 12 Oct 2016; accepted 13 Oct 2016; published 19 Oct 2016

Biomedical Optics EXPRESS

surface characteristics of hard dental tissues ablated with ArF pulsed excimer lasers," Lasers Surg. Med. **11**(6), 499–510 (1991).
10. M. H. Niemz, A. Kasenbacher, M. Strassl, A. Bäcker, A. Beyertt, D. Nickel, and A. Giesen, "Tooth ablation using a CPA-free thin disk femtosecond laser system," Appl. Phys. B **79**(3), 269–271 (2004).
11. A. V. Rode, E. G. Gamaly, B. Luther-Davies, B. T. Taylor, J. Dawes, A. Chan, R. M. Lowe, and P. Hannaford, "Subpicosecond laser ablation of dental enamel," J. Appl. Phys. **92**(4), 2153 (2002).
12. D. V. Palanker, M. S. Blumenkranz, D. Andersen, M. Wiltberger, G. Marcellino, P. Gooding, D. Angeley, G. Schuele, B. Woodley, M. Simoneau, N. J. Friedman, B. Seibel, J. Batlle, R. Feliz, J. Talamo, and W. Culbertson, "Femtosecond laser-assisted cataract surgery with integrated optical coherence tomography," Sci. Transl. Med. **2**(58), 58ra85 (2010).
13. C. L. Hoy, W. N. Everett, M. Yildirim, J. Kobler, S. M. Zeitels, and A. Ben-Yakar, "Towards endoscopic ultrafast laser microsurgery of vocal folds," J. Biomed. Opt. **17**(3), 038002 (2012).
14. M. Yildirim, O. Ferhanoglu, J. Kobler, S. M. Zeitels, and A. Ben-Yakar, "Parameters affecting ultrafast laser microsurgery of subepithelial voids for scar treatment in vocal folds," J. Biomed. Opt. **18**(11), 118001 (2013).
15. C. L. Hoy, O. Ferhanoglu, M. Yildirim, K. H. Kim, S. S. Karajanagi, K. M. C. Chan, J. B. Kobler, S. M. Zeitels, and A. Ben-Yakar, "Clinical Ultrafast Laser Surgery: Recent Advances and Future Directions," IEEE J. Sel. Top. Quantum Electron. **20**(2), 242–255 (2014).
16. S. M. Zeitels, A. Ben-Yakar, C. L. Hoy, W. N. Everett, J. B. Kobler, R. R. Anderson, W. A. Farinelli, "Systems, devices and methods for imaging and surgery," U.S. patent US2013/0211391 A1 (2013).
17. C. L. Hoy, N. J. Durr, P. Chen, W. Piyawattanametha, H. Ra, O. Solgaard, and A. Ben-Yakar, "Miniaturized probe for femtosecond laser microsurgery and two-photon imaging," Opt. Express **16**(13), 9996–10005 (2008).
18. C. L. Hoy, O. Ferhanoğlu, M. Yildirim, W. Piyawattanametha, H. Ra, O. Solgaard, and A. Ben-Yakar, "Optical design and imaging performance testing of a 9.6-mm diameter femtosecond laser microsurgery probe," Opt. Express **19**(11), 10536–10552 (2011).
19. O. Ferhanoglu, M. Yildirim, K. Subramanian, and A. Ben-Yakar, "A 5-mm piezo-scanning fiber device for high speed ultrafast laser microsurgery," Biomed. Opt. Express **5**(7), 2023–2036 (2014).
20. F. Couny, F. Benabid, P. J. Roberts, P. S. Light, and M. G. Raymer, "Generation and photonic guidance of multi-octave optical-frequency combs," Science **318**(5853), 1118–1121 (2007).
21. O. H. Heckl, C. J. Saraceno, C. R. E. Baer, T. Südmeyer, Y. Y. Wang, Y. Cheng, F. Benabid, and U. Keller, "Temporal pulse compression in a xenon-filled Kagome-type hollow-core photonic crystal fiber at high average power," Opt. Express **19**(20), 19142–19149 (2011).
22. Y. Y. Wang, N. V. Wheeler, F. Couny, P. J. Roberts, and F. Benabid, "Low loss broadband transmission in hypocycloid-core Kagome hollow-core photonic crystal fiber," Opt. Lett. **36**(5), 669–671 (2011).
23. F. Emaury, C. F. Dutin, C. J. Saraceno, M. Trant, O. H. Heckl, Y. Y. Wang, C. Schriber, F. Gerome, T. Südmeyer, F. Benabid, and U. Keller, "Beam delivery and pulse compression to sub-50 fs of a modelocked thin-disk laser in a gas-filled Kagome-type HC-PCF fiber," Opt. Express **21**(4), 4986–4994 (2013).
24. B. Beaudou, F. Gerôme, Y. Y. Wang, M. Alharbi, T. D. Bradley, G. Humbert, J.-L. Auguste, J.-M. Blondy, and F. Benabid, "Millijoule laser pulse delivery for spark ignition through kagome hollow-core fiber," Opt. Lett. **37**(9), 1430–1432 (2012).
25. Y. Y. Wang, X. Peng, M. Alharbi, C. F. Dutin, T. D. Bradley, F. Gérôme, M. Mielke, T. Booth, and F. Benabid, "Design and fabrication of hollow-core photonic crystal fibers for high-power ultrashort pulse transportation and pulse compression," Opt. Lett. **37**(15), 3111–3113 (2012).
26. A. Brodeur and S. L. Chin, "Ultrafast white-light continuum generation and self-focusing in transparent condensed media," J. Opt. Soc. Am. B **16**(4), 637 (1999).
27. J. H. Marburger, "Self-focusing: Theory," Prog. Quantum Electron. **4**, 35–110 (1975).
28. A. Shadfan, M. Pawlowski, Y. Wang, K. Subramanian, I. Gabay, A. Ben-Yakar, and T. Tkaczyk, "Design and fabrication of a miniature objective consisting of high refractive index zinc sulfide lenses for laser surgery," Opt. Eng. **55**(2), 025107 (2016).
29. M. Debenham, "Refractive indices of zinc sulfide in the 0.405-13-[mgr]m wavelength range," Appl. Opt. **23**(14), 2238 (1984).
30. T. D. Krauss and F. W. Wise, "Femtosecond measurement of nonlinear absorption and refraction in CdS, ZnSe, and ZnS," Appl. Phys. Lett. **65**(14), 1739 (1994).
31. J. He, Y. Qu, H. Li, J. Mi, and W. Ji, "Three-photon absorption in ZnO and ZnS crystals," Opt. Express **13**(23), 9235–9247 (2005).
32. B. Gu, J. He, W. Ji, and H. T. Wang, "Three-photon absorption saturation in ZnO and ZnS crystals," J. Appl. Phys. **103**(7), 9235–9247 (2008).
33. R. L. Sutherland, *Handbook of Nonlinear Optics* (1997), Vol. 36.
34. J. He, Y. Qu, H. Li, J. Mi, and W. Ji, "Three-photon absorption in ZnO and ZnS crystals," Opt. Express **13**(23), 9235–9247 (2005).
35. R. K. Jamal, M. T. Hussein, and A. M. Suhail, "Three-Photon Absorption in Zno Film Using Ultra Short Pulse Laser," J. Mod. Phys. **3**(08), 856–864 (2012).
36. A. Ben-Yakar and R. L. Byer, "Femtosecond laser ablation properties of borosilicate glass," J. Appl. Phys. **96**(9), 5316–5323 (2004).
37. K. Venkatakrishnan, B. Tan, and B. K. A. Ngoi, "Femtosecond pulsed laser ablation of thin gold film," Opt. Laser Technol. **34**(3), 199–202 (2002).

Biomedical Optics EXPRESS

38. H. Huang and Z. Guo, "Ultrashort pulsed laser ablation and stripping of freeze-dried dermis," Lasers Med. Sci. **25**(4), 517–524 (2010).
39. H. Huang and Z. Guo, "Human dermis separation via ultra-short pulsed laser plasma-mediated ablation," J. Phys. D Appl. Phys. **42**(16), 165204 (2009).
40. F. H. Loesel, J. P. Fischer, M. H. Gotz, C. Horvath, T. Juhasz, F. Noack, N. Suhm, and J. F. Bille, "Non-thermal ablation of neural tissue with femtosecond laser pulses," Appl. Phys. B Lasers Opt. **66**, 121–128 (1998).

1. Introduction

Tissue removal by ultrafast laser pulses is ideal for microsurgery since it offers a high degree of spatial and thermal confinement. When ultrafast pulses are tightly focused inside a dielectric medium, such as tissue, the high peak intensities in the focal volume can lead to spatially confined non-linear absorption [1]. Additionally, since the pulses interact with the medium in time scales faster than that needed for phonon-phonon coupling, these processes exhibit high thermal confinement during energy deposition [2]. These ablation characteristics allow for extremely precise tissue removal with minimal damage to the surrounding tissue. Substantial research efforts over the last two decades have explored tissue ablation in the corneal stroma [3–5], cortical parenchyma [6], and epidermis [7], and harder tissue like nail [8] and dentin [9–11]. These studies led to the first clinical use of ultrafast lasers in laser assisted in situ keratomileusis (LASIK) for flap creation [3] and more recently for cataract surgery [12].

With the unique ability to ablate a few hundred microns underneath the tissue surface without harming the superficial layers, ultrashort pulse lasers hold promise in developing new treatment modalities and methodologies, such as those proposed for the treatment of scarred vocal folds [13–15]. However, the clinical adoption of ultrafast lasers for surgery has been restricted to ophthalmic surgery. One reason is the easy access to the eyes, which has facilitated direct, free space delivery of ultrafast pulses in ophthalmic surgeries using external microscope setups. To utilize this laser surgery method at other organs within the human body, there is a need for a compact and flexible surgery system that can deliver these high intensity pulses to the target site. A second reason that limits widespread adoption of these lasers is the higher optical scattering properties of most other tissues like skin and muscle, which necessitate micro-Joules of energy delivery through optical fibers for performing surgeries below the surface.

Recent developments in the field of hollow-core, photonic crystal fibers have brought us closer to clinically viable, handheld ultrafast laser surgery devices. Taking advantage of this new type of fibers, our group has led the development of several versions of ultrafast laser scalpels with selective cell and tissue surgery capabilities [16]. Over the course of 10 years, we developed 3 generations of probes, progressively decreasing the cross sectional diameter from 18 mm [17] to 9.6 mm [18] and finally to 5 mm [19]. Using hollow-core photonic bandgap fibers (HC-PBF) and pre-chirping 100 fs pulses to 11.5 ps to pre-compensate for fiber dispersion, allowed us to deliver higher pulse energies without damaging the fiber, thanks to the increased ablation threshold at longer pulse-widths. Consequently, we were able to transmit laser pulses of close to 1.6 μJ energy through the fiber and 0.35 μJ through the entire probe [17]. Aiming to increase surgery speeds in our third generation probe, we used a higher repetition rate (300 kHz) fiber laser, which allowed us to drill through a 70 μm thick tissue slice over a 150 × 150 μm^2 scan area in about 10 seconds. Theoretical calculations revealed that the probe could be moved linearly along the tissue surface at translation speeds of 4 mm/s [19] while covering up to 80% of the scan area by at least one laser pulse. Although the fiber laser's narrow bandwidth prevented pre-chirping of the pulse, we still achieved a 5-fold improvement in the overall transmission of the probe by replacing the lossy and bulky MEMS scanning mirror elements with resonant fiber tip scanning instead. As a result, the in-line architecture of our third-generation probe nearly doubled the overall energy delivery of the first generation probes.

Biomedical Optics EXPRESS

The development of the third generation probe also shed light on a number of issues that could limit the clinical applicability of small core size HC-PBF fibers. We established that the cladding damage at the input face of the fiber was the limiting factor for the maximum energy deliverable through HC-PBF fibers. The cladding damage occurs when the fluence at the tail of the beam reaches the silica damage threshold at the coupling face. Small axial and radial coupling misalignments and Poynting vector instabilities of the fiber laser can cause beam displacement and further reduce the threshold of fluence that can damage the cladding. As a result, we found that the small core sizes of HC-PBFs limited their energy delivery to about 700 nJ in our case. Additionally, these fibers suffer from large spatial overlap of the core mode with the silica core wall, which also limits the maximum energy deliverable.

A possible solution to the limited energy delivery problem lay in the development of a new class of Kagome lattice hollow-core photonic crystal fibers, exhibiting properties suitable for high energy pulse delivery [20]. These Kagome fibers guide light based on inhibited coupling (IC) between the core and cladding modes. The IC results in reduced spatial overlap of the core mode with the silica walls allowing substantially higher pulse energies to be delivered at the expense of increased attenuation (> 0.5 dB/m). The Kagome lattice structure also accommodates larger core diameters. As a result, Kagome fibers have been shown to deliver single-mode pulse energies of up to 10 μJ at 800 nm in vacuum [21]. Recently Kagome fibers with a hypocycloid core geometry were shown to exhibit low loss comparable to HC-PBFs (~180 dB/km) over broadband transmission [22,23], thanks to the enhanced IC between the core and cladding modes. In subsequent work, transmission of pulse energies as high as 100 μJ was demonstrated [24,25] in fibers filled with Helium to avoid nonlinear effects. Despite relatively larger core sizes compared to other hollow core photonic crystal fibers, the Kagome fiber also maintained single mode delivery. These hypocycloid Kagome lattice fibers exhibit excellent characteristics for ultra-short pulse beam delivery with ultra-low optical attenuation and configurable dispersion characteristics.

Taking these advantages of large hollow-core Kagome fibers, we developed a new endoscopic laser scalpel that can deliver micro-Joules of energy at the tissue over a scan area of 75 × 75 μm^2. The optical design of the scalpel brought with it new challenges in accommodating the small fiber NA. We specially designed an objective with lenses made of a high refractive index material, Zinc-Sulfide (ZnS) crystal, to increase the focusing NA while maintaining telecentric operation over the scanning field of view (FOV). This paper presents the design and development of this piezo-scanning fiber scalpel, its performance characterization, and the high-speed microsurgery results in *ex vivo* tissue samples. Additionally, we characterize the onset of nonlinear properties of Zinc Sulfide (ZnS) to understand the feasibility and limitations of using high refractive index materials for miniaturized optics in ultrafast laser applications.

2. Design and selection of critical components

2.1 Overall design

The scalpel's design must meet a number of key requirements for clinical adoption, including a form factor small enough for endoscopic use and fast surgery speeds. In terms of the optics, focusing of ultrashort pulses is needed for initiating ablation on or inside the tissue. Additionally, beam steering is necessary to scan the micrometer size beam over an ablation FOV, to increase the surface area affected by the consecutive pulses per unit time.

We set the probe diameter to be approximately 5 mm to facilitate easy integration with existing oto-laryngological microsurgery systems. The scalpel's design incorporates an inline architecture that reduces the form factor of the device while increasing overall power transmission [19]. With this configuration, we could house all the components within a stainless steel casing with an outer diameter (OD) of 5.15 mm (Fig. 1(a)). We adopted a piezo-based Lissajous beam steering mechanism that vibrated a cantilevered fiber tip at the fundamental resonance frequency. The inherent, minor asymmetry in the mass of the

Biomedical Optics EXPRESS

overhanging fiber section naturally provided slightly different resonant frequencies in the x and y directions, yielding a quasi-repetitive Lissajous pattern. We chose scan frequencies close to 1 kHz by using a fiber overhang length of 10 mm, to assist the rapid coverage of the FOV and achieve fast translation speeds for the scalpel.

High-speed ablation can be achieved by using the new generation ultrafast fiber laser systems, which boast 10's of micro-Joule level pulse energies delivered at 100's kHz repetition rates. We previously showed that such high repetition rates would give surgeons the ability to move the surgery probes along the surface at ergonomic speeds of a few mm/s while producing an uninterrupted cut. For our experiments, we utilized an Erbium-doped fiber laser (1552 nm, 600 fs, 303 kHz, 2 W, Discovery, Raydiance) and frequency doubled it to operate at 776 nm and 1.5 ps, providing a maximum average power of 0.67 W (2.2 μJ pulse energies) available for delivery into our probe. Building on the advantages of the high repetition rate laser, we now aim to improve the volume of ablation by delivering increased pulse energies that will concomitantly enable increasing the ablation spot size.

The use of Kagome fibers enabled us to successfully transmit the full power available from our fiber laser. We specifically used a 31 μm mode field diameter (MFD) and hypocycloid core Kagome fiber (0.018 NA, PMC-PL-780-UP, GLOphotonics), shown in the inset of Fig. 1(b). The fiber exhibits near-zero group velocity dispersion (GVD) at our operating wavelength of 776 nm while exhibiting a broadband transmission from ~750 nm to 1400 nm (Fig. 1(b)).

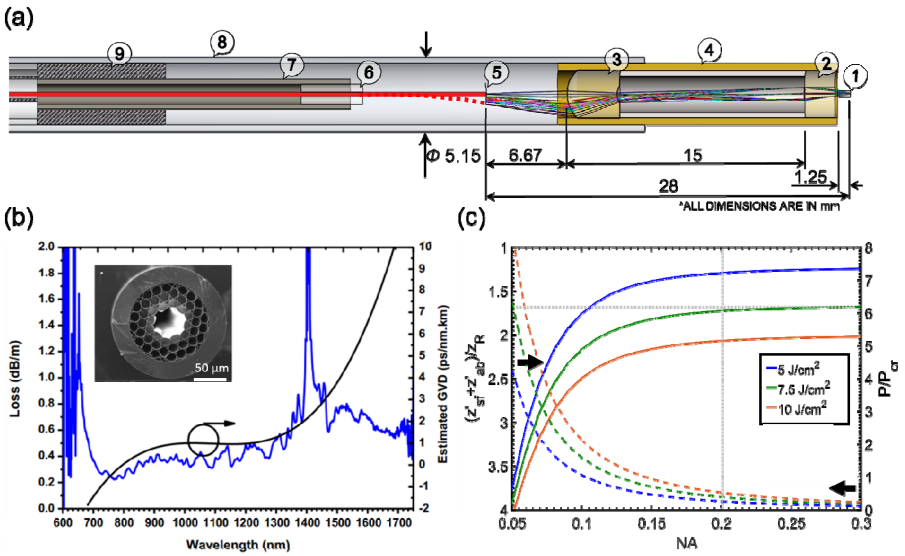

Fig. 1. Opto-mechanical design of the endoscopic scalpel. (a) A cross sectional view of the scalpel's design developed using Solidworks®, overlaid with optical design ray tracing generated in Zemax. The device focuses the laser onto the tissue surface (1) using a miniaturized objective piece made of a coverslip (2) and two ZnS lenses (3 & 4). The locus of the optic fiber tip (5) is mapped in Zemax to simulate the path of the rays from the focal plane back through the objective. A PMMA insert (6) holds the fiber within the inner cavity of a cylindrical piezo-electric actuator (7). The actuator is centered within an outer 304SS casing (8) using an accurately turned epoxy plug (9). The dashed red-line indicates fiber position at maximum deflection during scanning. (b) The broadband transmission spectra of the Kagome fiber and an SEM image (inset), showing its large, hypocycloid core geometry. (c) The normalized ablation plane shift from the theoretical focal plane, due to out-of-focus ablation and self-focusing for a range of operating fluences, at different NAs. The right axis of the plot shows the corresponding peak powers normalized with respect to the critical power for self-focusing in water. We performed the calculations for our design working distance of 900 μm. The NA of our final design is 0.23.

Biomedical Optics EXPRESS

The primary optical design criteria of the objective was achieving the highest focusing NA while enabling the largest possible scanning FOV and accommodating the low NA of the fiber (0.018). Specifically, at high peak intensities, the focusing NA needed to be high enough to avoid possible focal shift due self-focusing effects in water and more importantly out-of-focus ablation due to prematurely reaching the ablation threshold. To determine the effect of NA on self-focusing, we estimated the collapse distance in water due to self-focusing for a Gaussian beam, geometrically focused using a lens with a focal length f using [26]

$$z'_{sf} = \frac{z_{sf} f}{z_{sf} + f}, \tag{1}$$

where z_{sf} is the self-focusing collapse distance for a collimated Gaussian beam, given by [27]

$$z_{sf} = \frac{0.367ka^2}{\left\{\left[\left(\frac{P}{P_{crit}}\right)^{1/2} - 0.852\right]^2 - 0.0219\right\}^{1/2}}. \tag{2}$$

Here, ka^2 is the diffraction length, where k is the wave number in water and a is the $1/e^2$ beam radius of the beam at the entrance face of water, which we calculated based on the focusing NA and the chosen working distance of 900 µm. The term P is the peak power of the input beam, while P_{crit} refers to the self-focusing critical peak power given by

$$P_{crit} = \frac{3.77\lambda^2}{8\pi n_0 n_2}. \tag{3}$$

Here λ is the laser wavelength in vacuum, $n_0 = 1.33$ and $n_2 = 4.1\times10^{-16}$ cm^2/W are the linear and non-linear components of the intensity dependent refractive index of water [27].

We also estimated z'_{ab}, which represents the axial distance from the focal plane where the average fluence of the laser pulse reaches the ablation threshold for water, which was taken as 2 J/cm^2. Figure 1(c) presents the estimated total shift in terms of Rayleigh length as a function of the NA for input fluences of 5, 7.5, and 10 J/cm^2. These fluences represent several times the expected tissue ablation threshold [14]. At each fluence, we also calculated the corresponding peak powers. Our calculations for Fig. 1(c) indicate two distinct regimes. Below an NA of 0.15, the high peak powers needed to achieve the target fluence produce strong self-focusing and out-of–focus ablation. On the other hand, at NAs larger than 0.15, self-focusing effects are minimal, while the out-of-focus ablation in water becomes the dominant factor in shifting the ablation plane. We found that NA of 0.2 and upwards asymptotes to the smallest shift in the ablation plane, close to 1.4 times the theoretical Rayleigh length of the focal spot. Therefore, we used this NA value to guide our design where we can achieve the largest possible FOV, while minimizing out-of-focus ablation effects.

The size of the optical elements was limited to approximately 4 mm so that they could fit inside the 5-mm housing, while leaving sufficient wall thickness to keep the housing structurally strong. Meanwhile, the FOV on the tissue depended on the fiber tip deflection and inversely on the magnification of the objective. By driving a piezo-electric tube (PZT) at the resonant frequency of the extended fiber tip, we achieved a maximum tip deflection of ± 500 µm at 100 V applied voltage, which was 80% of the maximum allowable driving voltage for the PZT. For a 10 × magnification of the objective (for a 0.2 NA), we estimated a FOV of about 100 × 100 µm^2, which was large enough for a tissue cutting scalpel. In addition to these

Biomedical Optics EXPRESS

design parameters, our design also needed to ensure minimal vignetting of the FOV, and mechanical stability of all components.

2.2 Miniaturized objective design

The need for tight focusing of laser beams, delivered through a low NA fiber, necessitated development of a custom objective [28]. We used the Zemax® optical design package for the design, optimization, and tolerance analysis. The optical system was designed in reverse, with the tissue side space simulated as flat object and the curved trajectory of the fiber tip modeled as the image space, with a radius of 6.6 mm. The final objective comprised of two 4-mm diameter lenses made from multispectral Zinc Sulfide (ZnS), an optically transparent semiconductor crystal with a high refractive index of 2.32 at 780 nm [29]. The use of custom designed ZnS lenses allowed for the aspherization of all active optical surfaces, to minimize FOV curvature. Figure 1(a) shows the simulated rays, launching along the locus of the fiber tip as it deflects by the piezo actuation. While the large refractive index of ZnS provided a compact objective design, its nonlinear absorption properties at high peak intensities lead to undesirable effects such as reduced transmission and changing focusing conditions. Therefore, we carefully assessed the nonlinear absorption properties of our objective, which we describe in the subsequent section.

The design produced an objective with NA of 0.23 when the probe tip is immersed in water and a working distance of 900 μm from the cover slip, meeting our design specifications. Under a paraxial approximation and taking into account beam truncation effects, Zemax simulations estimated a $1/e^2$ focused spot diameter of 3.8 μm along the optical axis with a Strehl ratio of 0.99, which was maintained across the entire FOV [28]. Focusing in air on to the tissue surface slightly increased the spot size estimate to 3.88 μm. The objective design positioned the fiber tip 6.7 mm away from the back surface of the objective to accommodate the rays from the scanning fiber tip. We expect a flat, 77×77 μm^2 FOV for the ± 500 μm fiber tip deflection for the 13 × demagnification of the objective. We assessed the performance of the objective by imaging USAF resolution targets and the measurement of the Strehl ratio over the entire optical field [28]. The objective was able to resolve group 8, element 5 on the USAF chart, meeting expected diffraction-limited performance requirements. Damage to the lens and the anti-reflective coatings, however, resulted in a Strehl ratio of 0.55 for the objective.

2.3 Manufacturing and packaging

The lenses used in the objective were manufactured by single-point diamond turning ZnS pellets to the desired specifications [28]. Near infrared (NIR) anti-reflection coatings (refractory oxide coating, Optical Filter Source LLC) were applied to the lenses of the objective to counteract the Fresnel reflections off these high refractive index lenses. The coatings were expected to provide less than 1% reflectance at the laser wavelength of 776 nm. We packaged the lenses within a thin walled brass tube of OD = 4.8 mm and used hollow, cylindrical spacers to set the distance between the optical elements.

For the housing of the objective along with the other components of the scalpel, we used a 6X gauge size hypodermic tube with an inner diameter of ID = 4.80 mm and OD = 5.15 mm (Fig. 1(a)). The inner surface of the hypodermic tube acted as datum to align all mechanical and optical components accurately. Diamond turning of all cylindrical surfaces with a turning lathe provided micron level accuracy. For the PZT (EBL products Inc.), electrical connections were soldered to the four quadrants and ground. To electrically isolate the connections and to accurately fit the PZT into the housing, we applied a quick set epoxy glue over the electric connects and turned to match the ID of the housing. For mounting the optical fiber within the hollow center of the PZT, we specially machined a 1-mm long glass insert with an OD matching the ID of the PZT and a hole at its center to support the fiber while providing a clearance fit to the fiber's jacket. After cleaving the fiber, we adjusted the overhang length of

Biomedical Optics EXPRESS

the fiber as per our design specifications with an accuracy of ± 0.5 mm. The distance between the fiber tip and the objective is adjusted using spacers manufactured from 6.5-gauge size hypodermic tubing.

3. Results and discussion

3.1 Optical characterization of the probe

The laser source can be efficiently coupled to the Kagome fiber by matching the NA of the coupling lens to the fiber NA according to

$$f = d_{coll} \cdot \frac{\pi d_{mf}}{4\lambda}, \tag{4}$$

where d_{coll} is the $1/e^2$ diameter of the collimated laser beam and $d_{mf} = 31\,\mu m$ is the fiber MFD. We measured the $1/e^2$ diameter of our laser to be 6.75 mm, which led us to use a 200 mm focal length coupling lens. We adjusted the fiber tip position using a 5-axis translational stage to achieve single mode transmission through the fiber. To obtain visual feedback for the alignment, we imaged the beam at the distal end of the fiber using a 10 × objective (0.28 NA, Plan Apo, Mitutoyo) and a beam profiler (UNIQ, Ophir Optronics). The coupling efficiency of the fiber was 91%, as determined by the ratio of the output to input power of 85% and fiber transmission efficiency of 94% (–0.25 dB/m).

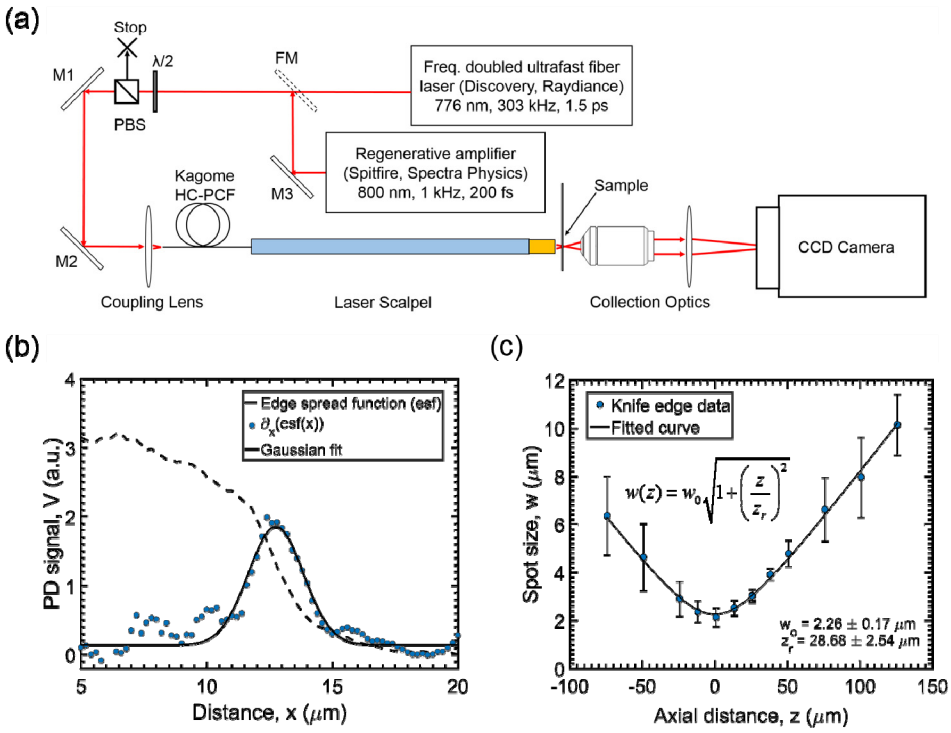

Fig. 2. Optical characterization of the probe. (a) The optical setup used for probe characterization and ablation studies. The fiber laser is used for all ablation experiments, while the regenerative amplifier system is used to test the nonlinear characteristics of the ZnS lenses over a range of pulse widths. (b) An example plot of the measured lateral edge spread function and the Gaussian fit for determining the spot size at the focal plane through focusing in air. (c) Measured axial variation of spot size in air and corresponding estimates of lateral spot size and Rayleigh range from the curve fits.

Biomedical Optics EXPRESS

The pre-packaged miniaturized objective was inserted into the probe tip after fiber coupling was completed. The overall transmission efficiency of the probe was measured to be 62%, which was lower than the expected 75% of transmission, considering the total fiber coupling/transmission efficiency of 85% and the expected 12% reflective Fresnel losses at 6 surfaces in the 2 lenses of the objective and a cover slip. The additional losses are probably due to damage to the ZnS lenses, which occurred during the anti-reflection coating process.

To characterize the probe's performance, we used the setup shown in Fig. 2(a). While the objective was designed for water immersion, the comparatively low objective NA of 0.23 allowed us to characterize it in a simpler setup in air without deteriorating the focusing conditions substantially. We determined the focused spot size of the scalpel through knife-edge measurements. Beam sizes at different planes in the near and far field of the of the probe's focus were determined by differentiating the edge spread function, obtained from knife-edge measurements. Fitting the spot sizes to the Gaussian beam divergence equation revealed a focal $1/e^2$ diameter of 4.52 ± 0.17 µm (Fig. 2(b)). This spot size was 16% larger than the expected 3.88 µm design diameter in air. The Rayleigh range of focus was determined to be 57.4 ± 2.5 µm (Fig. 2(c)), which also slightly exceeded the theoretical value of 40.0 ± 0.4 µm in air.

The chosen operating frequencies for the two orthogonal axes of the fiber tip were 1187 Hz and 1203 Hz, as measured by scanning the sinusoidal driving voltage frequencies of the PZT around the theoretical resonant frequency of 1 kHz. A driving voltage of 100 V for each piezo quadrant resulted in a tip deflection of ± 500 µm to produce a maximal scanning FOV of 75 × 75 μm^2, and closely matching the expected FOV.

3.2 Maximum pulse energy deliverable through the probe and nonlinear effects

To characterize the Kagome fiber and the probe for pulse energies beyond the 2.2 µJ available from our fiber laser system at coupling, we used a regenerative amplifier system (803 nm, 1 kHz, Spitfire, Spectra Physics) to deliver larger pulse energies at varying pulse widths. As expected, Kagome fiber itself could deliver much larger pulse energies showing linear transmission even for the shortest pulse duration of 220 fs (Fig. 3(a)). However, the transmission through the entire probe deviated from this linear behavior at pulse-widths 1.5 ps and lower. The fiber does not produce any significant chirp thanks to its low GVD values that are smaller than ± 0.1 ps/mm.km in the wavelength range of 750 – 800 nm.

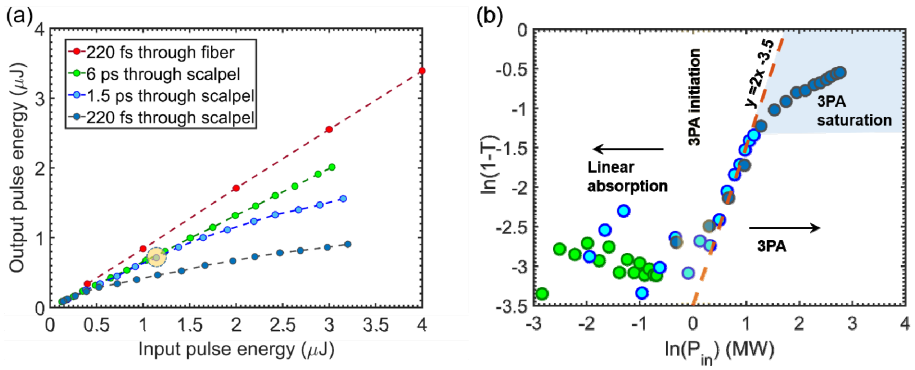

Fig. 3. Characterization of nonlinear absorption through the probe including miniaturized objective made of two ZnS lenses. (a) Measured transmission curves of 1-m Kagome fiber for 220 fs pulses and for the entire scalpel for 3 different pulse-widths. At the fiber laser's pulse-width of 1.5 ps, the objective exhibits linear operation up to ~1.4 µJ input pulse energies. (b) Linear fit to the logarithmic relationship between (1-Transmittance) versus input peak power for scalpel data presented in (a). The fit has a slope of two corresponding to a 3PA process according to Eq. (10). At powers below the 3PA threshold, only linear absorption is experienced. The device produces best results when operated in this linear range. At higher powers, saturation effects come into play for the 3PA process.

Biomedical Optics EXPRESS

We associated the optical limiting behavior of the objective lenses to possible nonlinear absorption in the ZnS lenses. Zinc Sulphide is a semiconductor with a band gap energy (E_g) close to 3.7 eV. Although it possesses an optically favorable high refractive index and a low linear absorption coefficient at NIR wavelengths, both two and three photon absorption (3PA) have been previously observed in ZnS crystals [30–32]. For NIR wavelengths (700 – 900 nm), the photon energies are less than $0.5E_g$ implying that nonlinear absorption should primarily stem from 3-photon processes. To test our hypothesis, we followed an analysis similar to that used in z-scan measurements for the estimation of nonlinear absorption parameters [33,34]. If we consider the variation of intensity I of a plane wave in ZnS with a linear absorption coefficient α and 3PA coefficient γ given by

$$\frac{dI}{dz} = -\alpha I - \gamma I^3 - \sigma_a N_{e-h} I, \tag{5}$$

where σ_a and N_{e-h} are the absorptive cross section and number density of the photo-excited charge carriers, respectively. By ignoring the charge carrier term and normalizing for linear absorption, we can analytically solve Eq. (5) for an expression describing the 3PA process. If we consider a setup where a lens with long Rayleigh range focuses laser pulses with a spatial and temporal Gaussian profile onto a thin semiconductor sample, the normalized energy transmittance $T(z)$ for 3PA can be derived from Eq. (5) [33]

$$T(z) = \frac{1}{\psi_0(z)\sqrt{\pi}} \int_{-\infty}^{\infty} \ln\left\{\sqrt{1+\psi_0^2(z)\cdot\exp(-2x^2)} + \psi_0(z)\cdot\exp(-x^2)\right\} dx, \tag{6}$$

with

$$\psi_0(z) = \left\{\frac{\gamma I_0^2}{1+(z/z_r)^2}\cdot\left(\frac{1-\exp(-2\alpha L)}{\alpha}\right)\right\}^{1/2}. \tag{7}$$

Here I_0 is the peak intensity at the focus of the lens, L is the length of the semiconductor sample, and z_r represents the Rayleigh range. If terms inside the square root are smaller than 1, Eq. (6) can be expanded using a Taylor's series. If we ignore the higher order terms, the transmission, normalized by the amount of linear absorption, can be expressed as [33,34]

$$T(z) = 1 - \frac{\gamma I_0^2 L_{eff}}{3^{3/2}\left\{1+(z/z_r)^2\right\}^2}, \tag{8}$$

where $L_{eff} = \left[1-\exp(-2\alpha_0 L)\right]/2\alpha_0$. To apply this model to our objective's transmission measurements, we can approximate the 2-lens objective to a single representative, stationary ZnS crystal and set z to zero in Eq. (8). We can then represent the normalized transmission in terms of input peak power (P_{in}). Since L_{eff}, γ, and the beam area, A, at input face are all constants, the normalized transmission T can be reduced to

$$T = 1 - \frac{\gamma P_{in}^2 L_{eff}}{3^{3/2}\cdot A^2} = 1 - \eta P_{in}^2 m, \tag{9}$$

where η is a constant that is specific to the optical configuration of our system (depending on the beam size and specific thickness of the lenses). Figure 3(b) shows a logarithmic plot of ($1-T$) vs. P_{in} that varies linearly with the onset of nonlinear absorption. The slope of two for this line establishes that we are indeed observing a 3PA process. The measurements deviate from

Biomedical Optics EXPRESS

this linear fit at low and high powers. At low powers, the transmittance is relatively constant as expected, since there is no 3PA. At higher powers, the slow asymptotic behavior of the transmittance curve can be explained by the loss of power to the photo-luminescence process [35] and onset of 3PA saturation [32].

For a more accurate analysis, we also need to take into account the self-focusing effects in ZnS ($n_2 = 0.75 \times 10^{-14}$ cm^2/W) [31], whose critical peak power is only about 0.12 MW. Self-focusing effects can hasten both the 3PA processes and eventually result in critical damage of the material. For our optical design, the self-focusing effects should be most dominant in lens element # 3 (Fig. 1(a)), where the beam size on the entrance face of the lens is smallest amongst the two lenses. However, the lens is only 4 mm thick, with a sharply concave second surface. These design features mitigate the self-focusing effects at our operating powers. However, for higher powers, an optical re-design with lens materials with lower n_2 will be prudent.

3.3 Characterization of FOV and ablation pattern across the FOV

We characterized the size of the FOV and ablation quality over the FOV by performing gold ablation studies, using the same setup used for knife-edge measurements. The knife was replaced by a sample that was prepared by sputter coating a 15 nm layer of gold onto a cover glass. We positioned the gold layer facing the laser scalpel and imaged the gold surface through the cover glass to the CCD camera via a 40 × objective. The probe was mounted on a translational stage and slowly brought forward until the focal point was also focused on the CCD camera, indicating that the focal spot and gold film were co-located at the same plane. The time window for laser ablation was controlled using a mechanical shutter (SH05, Thorlabs).

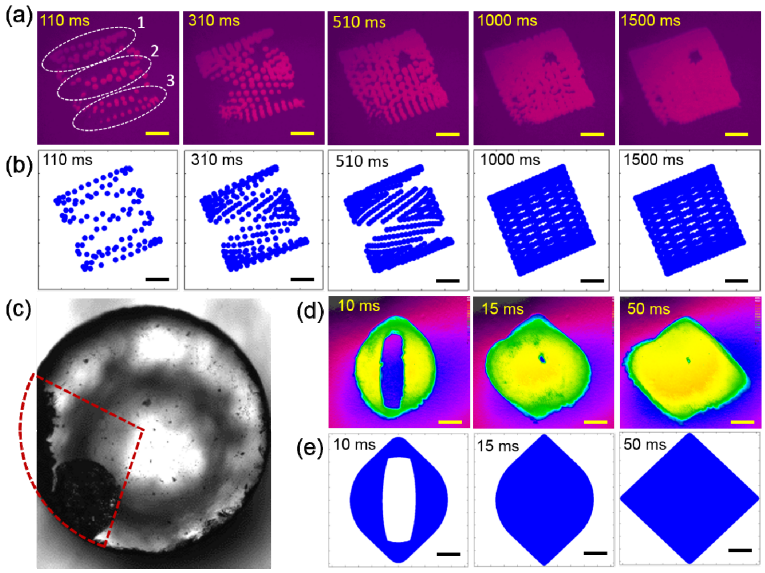

Fig. 4. Characterization of the FOV and ablation across the FOV. (a) Experimentally obtained ablation patterns on gold thin film sample over different time windows using 0.75 J/cm^2 pulses. Ablation spot sizes were larger at the center (region 2) and top (region 1) than the bottom of the FOV (region 3). The size of the measured FOV was 75 × 75 μm^2. (b) Simulation for Lissajous scanning taking into account the probe x and y scanning frequencies shows a slowly evolving ablation pattern for a 1 kHz laser repetition rate. (c) The ZnS lens #2 fiber-side surface after NIR coating process showing peripheral damage. The quadrant that is most affected is demarcated with a red dashed line. (d) Experimental results for ablation of gold sample at 303 kHz repetition rate for different time windows. (e) Corresponding simulations of ablation pattern. Scale bars represent 20 μm.

Biomedical Optics EXPRESS

To study the evolution of the ablation pattern over time and characterize the uniformity of the ablation spots across the FOV, we used the low repetition rate (1kHz) Ti:sapphire laser, which produced individual ablation spots that slowly sampled the Lissajous pattern (Fig. 4(a)). The FOV of the sampled region produced by these pulses measured 75 × 75 μm^2, closely matching the expected values (Fig. 4(b)). Over short time windows, the under-sampled pattern of ablation spots clearly highlighted the shape of the ablation spots across the entire FOV.

These experiments also allowed us to determine the gold ablation threshold based on the size of the ablation spot diameter D using the relation [36]

$$D^2 = 2w_0^2 \ln\left(\frac{F_{peak}}{F_{th}}\right), \tag{10}$$

where w_0 is the focal spot size of the laser on the surface, F_{peak} is the input peak fluence and F_{th} is the single-shot threshold fluence. We measured the size of the ablation spots at the center of the FOV for a range of input fluences. A linear curve fit to D^2 plotted as a function of logarithmic F_{peak} yielded a spot size of $2w_0 = 4.2 \pm 2.2$ μm, in line with our focal spot size measurements, and a threshold fluence of $F_{th} = 0.10 \pm 0.07$ J/cm^2, which compares favorably to previous studies [37].

Figure 4 shows ablation results for 0.75 J/cm^2, which is 7 times the fluence threshold for gold ablation. As would be expected, the higher fluences produced ablation spots larger than the measured laser spot size in the center of the FOV (Fig. 4(a)). The ablation spots were nearly circular over the entire FOV with larger spots in the center (4.78 ± 0.43 μm) and top (4.38 ± 0.09 μm) of the FOV than the bottom of the FOV (3.54 ± 0.25 μm). The variation in observed ablation spots can be attributed to varying fluence across the FOV due to changing spot size at the sample surface and variation of energy transmission across the clear aperture of the objective. Field curvature aberrations, astigmatism, and misalignments between the fiber and objective optical axes may be exacerbating the increase in the peripheral spot size distribution. We, however, strongly suspected reduced transmission to be the dominant cause for the non-uniform ablation spots, brought about by the damage to the lenses due to the coating process. The damage was predominantly confined to the lens periphery, with substantial damage to one quadrant of the lens face (Fig. 4(c)). Correspondingly, we see that the ablation spot size in region 3 (Fig. 4(a)) diminishes towards one side to such an extent that there are no ablation spots in the lower left corner of the FOV despite fluences over 7 times the threshold for gold ablation. Similar imperfections also seem to produce an un-ablated spot in the upper corner of the FOV as it becomes visible over increased exposure times. While this un-ablated spot should not affect material removal during translation of the probe, the reduced transmission along the edges will reduce the ablated area for materials with higher ablation thresholds, like tissue.

We modeled the ablation pattern assuming an ablation spot sized equal to the measured 4.52 μm focal spot size of the laser. Increasing the time window increased the FOV fill factor up to a theoretical saturation limit in our simulations (Fig. 4(b)).

Finally, we coupled the scalpel to our high-repetition rate fiber laser (303 kHz) to characterize the speed of ablation coverage of the FOV. Full coverage of the FOV was observed after 50 ms (Fig. 4(d)), in agreement with the theoretical model (Fig. 4(e)) and our previous studies [19].

3.4 High speed tissue ablation and material removal rate

To study the tissue ablation properties of the scalpel, we prepared 100 μm thick tissue slices from fresh porcine vocal fold tissue using cryostat sectioning. The wax free tissue samples were then embedded on a microscope slide, and stored at −20°C using a procedure described

Biomedical Optics EXPRESS

in earlier work [14]. We placed the tissue samples facing the laser scalpel and positioned them at the focal plane of the probe by imaging through their thickness using a 10 × objective (UPlanFL N, Olympus). For these experiments, we used the maximum deliverable fluence of 7.8 J/cm^2 at the focal plane with our current fiber laser system. The external mechanical shutter controlled the delivery of laser pulses that were synchronized to arrive on the tissue surface as the sample began translating using a custom LabView program. The motorized stage could translate the sample at a maximum speed of 5 mm/s. The high torque stepper motor of the stage could accelerate the sample to the set translational speeds within a short distance of 2 µm. Hence, the effects of the stage slowing down during direction changes of the stage were deemed negligible.

Figure 5(a) shows trenches that were formed by a single back and forth pass at translational speeds (u_c) ranging from 1 to 5 mm/s. A distinguishing feature of the ablation is the sinusoidal pattern along the edges of the trench, which becomes prominent at speeds of 3 mm/s and higher. These sampling artifacts arise from the interplay between Lissajous scanning and linear translation, which produces an alternating pattern of pulses that overlap at different rates. Seen clearly in our simulation results (Fig. 5(b)), the resulting wave pattern forms regions of increased pulse overlap that follows a sweeping sinusoidal curve along the direction of translation. The period of this sinusoidal curve is a function of translation speed. An increase in the translation velocity also decreases the width of this sinusoid, with a corresponding growth of the interspatial region of low sampling. Ablation is pronounced at regions experiencing higher number of overlapping pulses, i.e., along the sinusoid. At lower speeds, the crests of the wave pattern overlap to make ablation trench look rectangular. Higher speeds cause separation of the individual crests making them more discernable along the edges of the pattern. While, experimentally, u_c was limited to 5 mm/s, the maximum speed achievable with the stepper motor, our simulations pointed to a maximum cutting speed of ~8 mm/s that still enables sampling just under 100% of the target area.

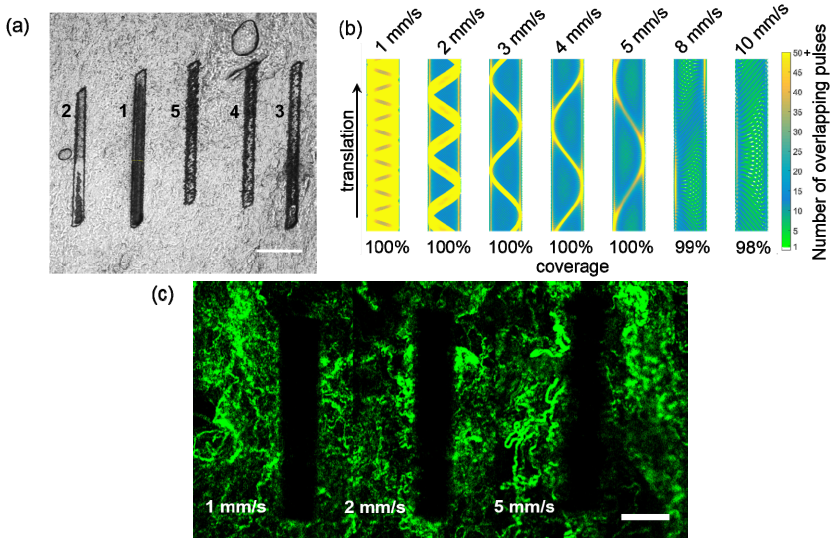

Fig. 5. Tissue surface ablation using the laser scalpel. (a) Images of 0.6 – 0.7 mm long ablation trenches in tissue using the scalpel. Numbers next to trenches represent translational speeds in mm/s. Scale bar represents 200 µm. (b) Simulation showing the effect of translational speed on ablation coverage. The sinusoidal overlapping pulse pattern produces uneven ablation at speeds less than 5 mm/s, due to the discrepancy between the number of pulses arriving at each spot. Higher speeds benefit from a more uniform distribution. (c) SHG microscopy images show signals from collagen structures and dark areas indicating 200 µm long, ~40 µm wide full depth trenches ablated by moving the samples back and forth at different translational speeds using fluence of 7.8 J/cm^2. Scale bar represents 50 µm.

Biomedical Optics EXPRESS

To calculate the material removal rate $\left(MRR = h_c \cdot b \cdot u_c\right)$ of the scalpel at our maximum operating fluence of 7.8 J/cm^2, we measured the cut depth (h_c) and the width (b) of the ablated trenches for different translation speeds (u_c). The tissue was completely removed for all speeds, resulting in an ablation depth of h_c = 43 ± 4 µm as assessed using an inverted microscope (IX73, Olympus). We believe that dehydration and collapse of the 100-µm tissue slices during freezing, storage, and defrosting, shrunk the tissue layer to its current thickness [38]. Second harmonic generation (SHG) images re-confirmed the cut dimensions. Figure 5(c) shows the top view SHG images of 200 µm long trenches ablated at different speeds. The tissue can be identified by the characteristic SHG signal of collagen fibers in the tissue. The dark regions lacking any SHG signal correspond to the ablated area. The trench widths were assessed to be between 40 - 45 µm wide, indicating that ablation only occurred across half the FOV of the objective. Narrower trench widths are most probably a result of the reduced transmission along the periphery of the damaged objective lenses. The 3D image stack confirmed that we had removed all of the tissue thickness in the trenches. We therefore set the depth of cut (h_c) as half the trench depth owing to the bi-directional sweep of the trench, namely 21.5 µm. For our cut width of 40 µm, we obtained an *MRR* of 0.26 mm^3/min using average powers of 0.4 W at the tissue surface.

To better interpret these numbers from a practical point of view, we calculated the time needed to remove a surface lesion of 5 mm in diameter. Assuming we cut around the lesion to separate it from the surface, we would make a series of 5 mm long cuts that are 20 – 25 µm deep, that covers the hemispherical area of the lesion. We estimate it would take ~4 minutes to remove the whole lesion with our microsurgery scalpel with the operating conditions mentioned above. It is clear that maximizing the *MRR* will allow surgeons to remove material quicker and reduce cutting time. Increasing the *MRR* should be possible by delivering larger average powers through the endoscope, either by increasing the pulse energies, the number of pulses, and/or the number of focused spots by using a bundle of Kagome fibers. Ultrafast fiber lasers with higher average powers are available as high as 50 W and should enable *MRR* > 30 mm^3/min.

Our simulations show that the high repetition rate laser produces between 7 and 40 consecutive overlapping pulses at a given location within the scan area for 5 mm/s cutting speed that we used in the experiments. The mean overlapping number of pulses is equal to 31, resulting in an average ablation rate of 0.7 µm/pulse. Similar ablation rates have been shown in dermis and brain tissue for similar fluence and pulse overlap conditions [39,40]. The simulations in Fig. 5(b) shows that faster translation speeds show more uniform ablation across the FOV, resulting in a more evenly ablated, albeit shallower pattern at higher speeds for each transition. A speed of 8 mm/s seems to provide the best combination of speed and coverage.

4. Conclusions

This study describes the development of our 4th generation endoscopic scalpel for ultrafast laser microsurgery. This latest iteration differentiates itself by using a specialized Kagome-lattice HC-PCF for micro-Joules level energy delivery and a custom objective to focus the low NA fiber output to achieve ablation. The final device could deliver all the available power from the current laser system reaching pulse energies of up to 1.2 µJ at the tissue. The objective optimally focused the low NA rays launching from the fiber to an NA of 0.23, thereby focusing the laser beam to a spot size of 4.38 um, while mitigating potential shift of the focused spot due to the self-focusing in water. The corresponding maximum fluence of 7.8 J/cm^2 was a few times larger than the tissue ablation threshold, providing sufficient intensities for rapid material removal rate. Sub-frame rate Lissajous scanning of the fiber tip to deliver the 303 kHz laser pulses allowed for high cutting speed ablation of tissue. We successfully demonstrated ablation of a 75 × 75 µm^2 FOV within 50 ms in gold, and showed

Biomedical Optics EXPRESS

surgery speeds of 5 mm/s in the ablation of 40 μm wide and 43 μm deep trenches in vocal fold tissue.

The challenging task of focusing the low NA fiber output to high NA necessitated a careful design of optical elements with a high refractive index material, ZnS. The design needs to ensure that the intensities through the ZnS crystal do not reach values high enough to introduce nonlinear effects. Transmission measurements confirmed linear operation over the entire working range of our 303 kHz fiber laser. The probe was capable of delivering the maximum available pulse energies of 1.2 μJ, which was substantially higher than our previous device, which was limited to ~450 nJ [19]. The improved delivery capabilities allowed us to maintain the fluence on the tissue surface achieved with our previous generation probe [19], for a larger ablation spot size. The benefits of the improved ablation spot size include increased ablation volume and improved coverage during scanning. However, the high non-linear susceptibility of ZnS limited its usefulness as a high refractive index optical material for use in ultrafast laser surgery probes, as we found that three-photon absorption takes over beyond 1.4 μJ pulse energies at our specific operating conditions. In our future designs, we will explore broadband CaF_2 optical crystals, which can be a better alternative to mitigate nonlinear limiting behavior of the ZnS optics at the expense of lower index of refraction and increased difficulty with aberration corrections.

The ability to deliver ultrafast pulses with micro-Joules of energy through flexible fibers thanks to the large hollow-core of Kagome fibers opens up a host of possibilities towards developing robust ultrafast laser microsurgery systems. A robust operation of such devices without causing any damage to the delivery fibers is an important requirement for clinical viability. The scalpel can be particularly useful in precise, micron scale, surgical excision of polyps, cysts, lesions, and tumors. With sufficient energies to overcome tissue scattering, sub-surface ablation via an endoscopic device also becomes a real possibility.

Funding

National Institute of Health (NIH) (RO1-DC014783 and R21-EB015022); Cancer Prevention and Research Institute of Texas (CPRIT) (RP130412).

Acknowledgments

We thank Raydiance Inc. for the use of their Discovery fiber laser.